Megahertz OCT for ultrawide-field retinal imaging with a 1050nm Fourier domain mode-locked laser

Thomas Klein, Wolfgang Wieser, Christoph M. Eigenwillig, Benjamin R. Biedermann and Robert Huber*

Lehrstuhl für BioMolekulare Optik, Fakultät für Physik, Ludwig-Maximilians-Universität München, Oettingenstr. 67, 80538 München, Germany
**Robert.Huber@LMU.de*

Abstract: We demonstrate ultrahigh speed swept source retinal OCT imaging using a Fourier domain mode locked (FDML) laser. The laser uses a combination of a semiconductor optical amplifier and an ytterbium doped fiber amplifier to provide more than 50mW output power. The 1050nm FDML laser uses standard telecom fiber for the km long delay line instead of two orders of magnitude more expensive real single mode fiber. We investigate the influence of this "oligo-mode" fiber on the FDML laser performance. Two design configurations with 684,400 and 1,368,700 axial scans per second are investigated, 25x and 50x faster than current commercial instruments and more than 4x faster than previous single spot ophthalmic results. These high speeds enable the acquisition of densely sampled ultrawide-field data sets of the retina within a few seconds. Ultrawide-field data consisting of 1900 x 1900 A-scans with ~70° degrees angle of view are acquired within only 3 and 6 seconds using the different setups. Such OCT data sets, more than double as large as previously reported, are collapsed to a 4 megapixel high definition fundus image. We achieve good penetration into the choroid by hardware spectral shaping of the laser output. The axial resolution in tissue is 12µm (684kHz) and 19µm (1.37MHz). A series of new data processing and imaging extraction protocols, enabled by the ultrawide-field isotropic data sets, are presented. Dense isotropic sampling enables both, cross-sectional images along arbitrary coordinates and depth-resolved en-face fundus images. Additionally, we investigate how isotropic averaging compares to the averaging of cross-sections along the slow axis.

©2011 Optical Society of America

OCIS codes: (110.4500) Optical coherence tomography; (140.3600) Lasers, tunable; (170.5755) Retina scanning; (170.4470) Ophthalmology; (170.0110) Imaging systems; (170.4500) Optical coherence tomography.

References and links

1. D. Huang, E. A. Swanson, C. P. Lin, J. S. Schuman, W. G. Stinson, W. Chang, M. R. Hee, T. Flotte, K. Gregory, C. A. Puliafito, and J. G. Fujimoto, "Optical coherence tomography," Science **254**(5035), 1178–1181 (1991).
2. A. F. Fercher, C. K. Hitzenberger, W. Drexler, G. Kamp, and H. Sattmann, "In vivo optical coherence tomography," Am. J. Ophthalmol. **116**(1), 113–114 (1993).
3. E. A. Swanson, J. A. Izatt, M. R. Hee, D. Huang, C. P. Lin, J. S. Schuman, C. A. Puliafito, and J. G. Fujimoto, "In vivo retinal imaging by optical coherence tomography," Opt. Lett. **18**(21), 1864–1866 (1993).
4. M. E. J. van Velthoven, D. J. Faber, F. D. Verbraak, T. G. van Leeuwen, and M. D. de Smet, "Recent developments in optical coherence tomography for imaging the retina," Prog. Retin. Eye Res. **26**(1), 57–77 (2007).
5. L. M. Sakata, J. Deleon-Ortega, V. Sakata, and C. A. Girkin, "Optical coherence tomography of the retina and optic nerve - a review," Clin. Experiment. Ophthalmol. **37**(1), 90–99 (2009).
6. C. K. Hitzenberger, P. Trost, P. W. Lo, and Q. Y. Zhou, "Three-dimensional imaging of the human retina by high-speed optical coherence tomography," Opt. Express **11**(21), 2753–2761 (2003).

#139343 - $15.00 USD Received 7 Dec 2010; revised 17 Jan 2011; accepted 21 Jan 2011; published 2 Feb 2011

7. M. Choma, M. Sarunic, C. Yang, and J. Izatt, "Sensitivity advantage of swept source and Fourier domain optical coherence tomography," Opt. Express **11**(18), 2183–2189 (2003).
8. J. F. de Boer, B. Cense, B. H. Park, M. C. Pierce, G. J. Tearney, and B. E. Bouma, "Improved signal-to-noise ratio in spectral-domain compared with time-domain optical coherence tomography," Opt. Lett. **28**(21), 2067–2069 (2003).
9. R. Leitgeb, C. Hitzenberger, and A. Fercher, "Performance of fourier domain vs. time domain optical coherence tomography," Opt. Express **11**(8), 889–894 (2003).
10. M. Wojtkowski, T. Bajraszewski, P. Targowski, and A. Kowalczyk, "Real-time in vivo imaging by high-speed spectral optical coherence tomography," Opt. Lett. **28**(19), 1745–1747 (2003).
11. M. Wojtkowski, T. Bajraszewski, I. Gorczyńska, P. Targowski, A. Kowalczyk, W. Wasilewski, and C. Radzewicz, "Ophthalmic imaging by spectral optical coherence tomography," Am. J. Ophthalmol. **138**(3), 412–419 (2004).
12. S. Yun, G. Tearney, J. de Boer, N. Iftimia, and B. Bouma, "High-speed optical frequency-domain imaging," Opt. Express **11**(22), 2953–2963 (2003).
13. R. Huber, M. Wojtkowski, and J. G. Fujimoto, "Fourier Domain Mode Locking (FDML): A new laser operating regime and applications for optical coherence tomography," Opt. Express **14**(8), 3225–3237 (2006).
14. W. Wieser, B. R. Biedermann, T. Klein, C. M. Eigenwillig, and R. Huber, "Multi-Megahertz OCT: High quality 3D imaging at 20 million A-scans and 4.5 GVoxels per second," Opt. Express **18**(14), 14685–14704 (2010).
15. M. W. Jenkins, D. C. Adler, M. Gargesha, R. Huber, F. Rothenberg, J. Belding, M. Watanabe, D. L. Wilson, J. G. Fujimoto, and A. M. Rollins, "Ultrahigh-speed optical coherence tomography imaging and visualization of the embryonic avian heart using a buffered Fourier Domain Mode Locked laser," Opt. Express **15**(10), 6251–6267 (2007).
16. R. Leitgeb, L. Schmetterer, W. Drexler, A. Fercher, R. Zawadzki, and T. Bajraszewski, "Real-time assessment of retinal blood flow with ultrafast acquisition by color Doppler Fourier domain optical coherence tomography," Opt. Express **11**(23), 3116–3121 (2003).
17. B. White, M. Pierce, N. Nassif, B. Cense, B. Park, G. Tearney, B. Bouma, T. Chen, and J. de Boer, "In vivo dynamic human retinal blood flow imaging using ultra-high-speed spectral domain optical coherence tomography," Opt. Express **11**(25), 3490–3497 (2003).
18. B. Považay, B. Hofer, C. Torti, B. Hermann, A. R. Tumlinson, M. Esmaeelpour, C. A. Egan, A. C. Bird, and W. Drexler, "Impact of enhanced resolution, speed and penetration on three-dimensional retinal optical coherence tomography," Opt. Express **17**(5), 4134–4150 (2009).
19. V. J. Srinivasan, D. C. Adler, Y. L. Chen, I. Gorczynska, R. Huber, J. S. Duker, J. S. Schuman, and J. G. Fujimoto, "Ultrahigh-speed optical coherence tomography for three-dimensional and en face imaging of the retina and optic nerve head," Invest. Ophthalmol. Vis. Sci. **49**(11), 5103–5110 (2008).
20. A. Unterhuber, B. Považay, B. Hermann, H. Sattmann, A. Chavez-Pirson, and W. Drexler, "In vivo retinal optical coherence tomography at 1040 nm - enhanced penetration into the choroid," Opt. Express **13**(9), 3252–3258 (2005).
21. D. M. de Bruin, D. L. Burnes, J. Loewenstein, Y. Chen, S. Chang, T. C. Chen, D. D. Esmaili, and J. F. de Boer, "In vivo three-dimensional imaging of neovascular age-related macular degeneration using optical frequency domain imaging at 1050 nm," Invest. Ophthalmol. Vis. Sci. **49**(10), 4545–4552 (2008).
22. E. C. W. Lee, J. F. de Boer, M. Mujat, H. Lim, and S. H. Yun, "In vivo optical frequency domain imaging of human retina and choroid," Opt. Express **14**(10), 4403–4411 (2006).
23. Y. Yasuno, Y. Hong, S. Makita, M. Yamanari, M. Akiba, M. Miura, and T. Yatagai, "In vivo high-contrast imaging of deep posterior eye by 1-microm swept source optical coherence tomography and scattering optical coherence angiography," Opt. Express **15**(10), 6121–6139 (2007).
24. B. Považay, B. Hermann, B. Hofer, V. Kajić, E. Simpson, T. Bridgford, and W. Drexler, "Wide-field optical coherence Tomography of the Choroid in Vivo," Invest. Ophthalmol. Vis. Sci. **50**(4), 1856–1863 (2009).
25. B. Považay, B. Hermann, A. Unterhuber, B. Hofer, H. Sattmann, F. Zeiler, J. E. Morgan, C. Falkner-Radler, C. Glittenberg, S. Blinder, and W. Drexler, "Three-dimensional optical coherence tomography at 1050 nm versus 800 nm in retinal pathologies: enhanced performance and choroidal penetration in cataract patients," J. Biomed. Opt. **12**(4), 041211–041217 (2007).
26. K. Bizheva, R. Pflug, B. Hermann, B. Povazay, H. Sattmann, P. Qiu, E. Anger, H. Reitsamer, S. Popov, J. R. Taylor, A. Unterhuber, P. Ahnelt, and W. Drexler, "Optophysiology: depth-resolved probing of retinal physiology with functional ultrahigh-resolution optical coherence tomography," Proc. Natl. Acad. Sci. U.S.A. **103**(13), 5066–5071 (2006).
27. V. J. Srinivasan, M. Wojtkowski, J. G. Fujimoto, and J. S. Duker, "In vivo measurement of retinal physiology with high-speed ultrahigh-resolution optical coherence tomography," Opt. Lett. **31**(15), 2308–2310 (2006).
28. S. Hariri, A. A. Moayed, A. Dracopoulos, C. Hyun, S. Boyd, and K. Bizheva, "Limiting factors to the OCT axial resolution for in-vivo imaging of human and rodent retina in the 1060 nm wavelength range," Opt. Express **17**(26), 24304–24316 (2009).
29. Y. Chen, D. L. Burnes, M. de Bruin, M. Mujat, and J. F. de Boer, "Three-dimensional pointwise comparison of human retinal optical property at 845 and 1060 nm using optical frequency domain imaging," J. Biomed. Opt. **14**(2), 024016–024015 (2009).
30. Y. Wang, J. Nelson, Z. Chen, B. Reiser, R. Chuck, and R. Windeler, "Optimal wavelength for ultrahigh-resolution optical coherence tomography," Opt. Express **11**(12), 1411–1417 (2003).
31. B. Potsaid, I. Gorczynska, V. J. Srinivasan, Y. L. Chen, J. Jiang, A. Cable, and J. G. Fujimoto, "Ultrahigh speed spectral / Fourier domain OCT ophthalmic imaging at 70,000 to 312,500 axial scans per second," Opt. Express **16**(19), 15149–15169 (2008).

#139343 - $15.00 USD Received 7 Dec 2010; revised 17 Jan 2011; accepted 21 Jan 2011; published 2 Feb 2011
(C) 2011 OSA

32. B. Potsaid, B. Baumann, D. Huang, S. Barry, A. E. Cable, J. S. Schuman, J. S. Duker, and J. G. Fujimoto, "Ultrahigh speed 1050nm swept source/Fourier domain OCT retinal and anterior segment imaging at 100,000 to 400,000 axial scans per second," Opt. Express **18**(19), 20029–20048 (2010).
33. C. M. Eigenwillig, T. Klein, W. Wieser, B. R. Biedermann, and R. Huber, "Wavelength swept amplified spontaneous emission source for high speed retinal optical coherence tomography at 1060 nm," Journal of Biophotonics, n/a-n/a (2010).
34. T. Bonin, G. Franke, M. Hagen-Eggert, P. Koch, and G. Hüttmann, "In vivo Fourier-domain full-field OCT of the human retina with 1.5 million A-lines/s," Opt. Lett. **35**(20), 3432–3434 (2010).
35. A. Sakamoto, M. Hangai, and N. Yoshimura, "Spectral-domain optical coherence tomography with multiple B-scan averaging for enhanced imaging of retinal diseases," Ophthalmology **115**(6), 1071–1078, (2008).
36. S. Jiao, R. Knighton, X. Huang, G. Gregori, and C. Puliafito, "Simultaneous acquisition of sectional and fundus ophthalmic images with spectral-domain optical coherence tomography," Opt. Express **13**(2), 444–452 (2005).
37. S. Jiao, C. Wu, R. W. Knighton, G. Gregori, and C. A. Puliafito, "Registration of high-density cross sectional images to the fundus image in spectral-domain ophthalmic optical coherence tomography," Opt. Express **14**(8), 3368–3376 (2006).
38. I. Gorczynska, V. J. Srinivasan, L. N. Vuong, R. W. S. Chen, J. J. Liu, E. Reichel, M. Wojtkowski, J. S. Schuman, J. S. Duker, and J. G. Fujimoto, "Projection OCT fundus imaging for visualising outer retinal pathology in non-exudative age-related macular degeneration," Br. J. Ophthalmol. **93**(5), 603–609 (2009).
39. L. Kagemann, H. Ishikawa, G. Wollstein, M. Gabriele, and J. S. Schuman, "Visualization of 3-D high speed ultrahigh resolution optical coherence tomographic data identifies structures visible in 2D frames," Opt. Express **17**(5), 4208–4220 (2009).
40. S. Marschall, T. Klein, W. Wieser, B. R. Biedermann, K. Hsu, K. P. Hansen, B. Sumpf, K.-H. Hasler, G. Erbert, O. B. Jensen, C. Pedersen, R. Huber, and P. E. Andersen, "Fourier domain mode-locked swept source at 1050 nm based on a tapered amplifier," Opt. Express **18**(15), 15820–15831 (2010).
41. B. R. Biedermann, W. Wieser, C. M. Eigenwillig, T. Klein, and R. Huber, "Dispersion, coherence and noise of Fourier domain mode locked lasers," Opt. Express **17**(12), 9947–9961 (2009).
42. H. C. Lefevre, "Single-mode fibre fractional wave devices and polarisation controllers," Electron. Lett. **16**(20), 778–780 (1980).
43. R. Huber, D. C. Adler, V. J. Srinivasan, and J. G. Fujimoto, "Fourier domain mode locking at 1050 nm for ultra-high-speed optical coherence tomography of the human retina at 236,000 axial scans per second," Opt. Lett. **32**(14), 2049–2051 (2007).
44. D. Gloge, "Weakly guiding fibers," Appl. Opt. **10**(10), 2252–2258 (1971).
45. I. V. Hertel, W. Muller, and W. Stoll, "Kinematic model for oligo-mode action of a CW dye-laser," IEEE J. Quantum Electron. **13**(1), 6–9 (1977).
46. R. G. Lamont, K. O. Hill, and D. C. Johnson, "Tuned-port twin biconical-taper fiber splitters: fabrication from dissimilar low-mode-number fibers," Opt. Lett. **10**(1), 46–48 (1985).
47. S. Ramachandran, "Dispersion-tailored few-mode fibers: A versatile platform for in-fiber photonic devices," J. Lightwave Technol. **23**(11), 3426–3443 (2005).
48. R. Huber, D. C. Adler, and J. G. Fujimoto, "Buffered Fourier domain mode locking: Unidirectional swept laser sources for optical coherence tomography imaging at 370,000 lines/s," Opt. Lett. **31**(20), 2975–2977 (2006).
49. W.-Y. Oh, B. J. Vakoc, M. Shishkov, G. J. Tearney, and B. E. Bouma, ">400 kHz repetition rate wavelength-swept laser and application to high-speed optical frequency domain imaging," Opt. Lett. **35**(17), 2919–2921 (2010).
50. A. C. Akcay, J. P. Rolland, and J. M. Eichenholz, "Spectral shaping to improve the point spread function in optical coherence tomography," Opt. Lett. **28**(20), 1921–1923 (2003).
51. J. Gong, B. Liu, Y. L. Kim, Y. Liu, X. Li, and V. Backman, "Optimal spectral reshaping for resolution improvement in optical coherence tomography," Opt. Express **14**(13), 5909–5915 (2006).
52. W. Drexler, "Ultrahigh-resolution optical coherence tomography," J. Biomed. Opt. **9**(1), 47–74 (2004).
53. F. J. Harris, "On the Use of Windows for Harmonic Analysis with the Discrete Fourier Transform," Proc. IEEE **66**(1), 51–83 (1978).
54. C. M. Eigenwillig, B. R. Biedermann, G. Palte, and R. Huber, "K-space linear Fourier domain mode locked laser and applications for optical coherence tomography," Opt. Express **16**(12), 8916–8937 (2008).
55. L. Kou, D. Labrie, and P. Chylek, "Refractive indices of water and ice in the 0.65- to 2.5-μm spectral range," Appl. Opt. **32**(19), 3531–3540 (1993).
56. B. R. Biedermann, W. Wieser, C. M. Eigenwillig, G. Palte, D. C. Adler, V. J. Srinivasan, J. G. Fujimoto, and R. Huber, "Real time en face Fourier-domain optical coherence tomography with direct hardware frequency demodulation," Opt. Lett. **33**(21), 2556–2558 (2008).
57. A. G. Podoleanu, "Unbalanced versus balanced operation in an optical coherence tomography system," Appl. Opt. **39**(1), 173–182 (2000).
58. C. C. Rosa, and A. G. Podoleanu, "Limitation of the achievable signal-to-noise ratio in optical coherence tomography due to mismatch of the balanced Receiver," Appl. Opt. **43**(25), 4802–4815 (2004).
59. S. Moon, and D. Y. Kim, "Normalization detection scheme for high-speed optical frequency-domain imaging and reflectometry," Opt. Express **15**(23), 15129–15146 (2007).
60. Y. Chen, D. M. de Bruin, C. Kerbage, and J. F. de Boer, "Spectrally balanced detection for optical frequency domain imaging," Opt. Express **15**(25), 16390–16399 (2007).
61. A. M. Rollins, and J. A. Izatt, "Optimal interferometer designs for optical coherence tomography," Opt. Lett. **24**(21), 1484–1486 (1999).

#139343 - $15.00 USD Received 7 Dec 2010; revised 17 Jan 2011; accepted 21 Jan 2011; published 2 Feb 2011
(C) 2011 OSA

62. A. R. Tumlinson, B. Hofer, A. M. Winkler, B. Povazay, W. Drexler, and J. K. Barton, "Inherent homogenous media dispersion compensation in frequency domain optical coherence tomography by accurate k-sampling," Appl. Opt. **47**(5), 687–693 (2008).
63. M. Wojtkowski, V. Srinivasan, T. Ko, J. Fujimoto, A. Kowalczyk, and J. Duker, "Ultrahigh-resolution, high-speed, Fourier domain optical coherence tomography and methods for dispersion compensation," Opt. Express **12**(11), 2404–2422 (2004).
64. A. J. den Dekker, and A. van den Bos, "Resolution: a survey," J. Opt. Soc. Am. A **14**(3), 547–557 (1997).
65. R. Engbert, and R. Kliegl, "Microsaccades uncover the orientation of covert attention," Vision Res. **43**(9), 1035–1045 (2003).
66. American National Standards Institute, "American National Standard for Safe Use of Lasers, ANSI Z136.1", (2007).

1. Introduction

Optical coherence tomography (OCT) can provide cross-sectional images and three dimensional data sets of biological tissue *in vivo* [1]. In ophthalmology, OCT enables the investigation of the layered structure of the ocular fundus [2, 3]. OCT is already in clinical use for non-invasive imaging of the human retina, enabling identification of pathologies and monitoring of therapy [4, 5]. With time-domain OCT, axial scan rates are limited even with sophisticated scan protocols due to limited speed of the scanning delay line [6]. The introduction of Fourier domain (FD) techniques paved the way to higher imaging speeds, while providing superior sensitivity compared to the original time domain approach [7–11]. In FD-OCT, the interference spectrum generated by backscattered light from the sample and from a reference mirror is measured. This is usually implemented with either a broadband light source plus a spectrometer with a line scan camera (spectral domain OCT/SD-OCT [10]), or with a wavelength swept laser plus photo detector (swept source OCT/SS-OCT, also known as optical frequency domain imaging/OFDI [12]).

Fourier domain mode locking (FDML) [13] has recently enabled high quality SS-OCT imaging at unprecedented acquisition speeds of up to 4 x 5,200,000 axial scans per second [14]. Ultrahigh speed OCT imaging has distinct advantages over lower speed systems. First, transient dynamics of the sample can only be resolved at characteristic frequencies well below imaging speed. Higher imaging speed can both increase update rate and provide 3D instead of 2D information [15]. An increased axial scan rate also gives access to larger flow speeds in Doppler OCT [16, 17]. Second, for densely sampled data sets, the total number of axial scans scales quadratically with the lateral dimension of the sample. Thus the total acquisition time rises dramatically with increasing sample size. Whereas this might be no problem for *ex vivo* studies, *in vivo* OCT imaging acquisition times are usually restricted to a few seconds due to sample motion. Hence either images are restricted to small areas or dense sampling is not possible [18]. Third, dense sampling does not only increase the amount of recorded information, but it also allows for advanced averaging methods in post-processing [19]. This is a considerable advantage over other averaging methods that require fixing of the averaging area prior to data acquisition.

In contrast to the wavelength region around 850nm, commonly used for retinal OCT imaging, scattering is reduced in the 1050nm water window. Hence retinal OCT imaging at 1050nm provides increased penetration into the choroid [20–22]. This permits reconstruction of choroidal vessels [23], and allows for deeper penetration of depth-resolved en-face images of the fundus [18, 24]. Furthermore, the imaging performance is improved in cataract patients [25]. Another advantage of the 1050nm range for OCT is that the retina is not stimulated at these long wavelengths, which enables unperturbed OCT surveillance of retinal stimulation with visible light [26, 27]. The drawbacks of the 1050nm wavelength range are limited axial resolution due to water absorption [28] and slightly less contrast between retinal layers than at 850nm [29]. Although the best achievable axial resolution is limited when restricting the 1050nm spectrum to the water window, the *degradation of resolution* over depth caused by dispersion is lower at 1050nm compared to 850nm, due to the zero dispersion wavelength of water at ~1000nm [30].

At 850nm, the highest imaging speed is currently achieved in SD-OCT with fast line cameras, yielding speeds of up to 312,500 axial scans per second [31]. Around 1050nm, line

#139343 - $15.00 USD Received 7 Dec 2010; revised 17 Jan 2011; accepted 21 Jan 2011; published 2 Feb 2011
(C) 2011 OSA

scan cameras are currently restricted to readout speeds below 100kHz, and the highest axial scan rates of up to 2 x 200kHz where recently presented by Potsaid et. al. with a two-spot SS-OCT setup [32]. Until now, the highest axial scan rates with a single spot have been performed with an FDML laser based SS-OCT setup at up to 249kHz axial scan rate [19] and with a non-laser source at an equivalent line rate of 340kHz [33]. Recently, a swept source full-field setup achieved record axial line rates of 1.5MHz over a small volume [34]. Retinal imaging can benefit from advantages of ultrahigh speed OCT mentioned earlier: Averaging has been clinically proven to increase signal to noise ratio, hence improving ophthalmologists' ability to distinguish retinal structures [35]. Simultaneous acquisition of high-density cross-sectional and fundus images [36] over larger areas requires co-registration protocols, if the imaging speed is not high enough [37]. For ultrahigh-speed systems, depth resolved en-face reconstructions of the fundus become feasible [18, 24, 38, 39]. Nevertheless, dense isotropic sampling [18] restricted the imaged area to a ~30°x30° field of view, even for the fastest published systems so far [24, 32]. This restriction complicates direct comparison and co-registration with standard clinical methods. Clinical fundus cameras usually allow taking a 45° field of view, while lasers scanning ophthalmoscopes may produce even larger fields of view. For instance, the Optos Optomap SLO covers up to 200 internal degrees of the retina. Note that this corresponds to 100° field of view with the more common "external" notation used throughout this paper.

The paper is organized as follows. In the next section, the FDML laser swept source is presented and characterized, followed by the data acquisition setup in section 3. Subsequently, ultrahigh speed ultrawide-field retinal imaging with our setup is presented. In the conclusion, we give a brief discussion of the work.

2. FDML laser based swept source setup and characterization

2.1. FDML laser design considerations and cavity layout

While FDML lasers are the highest performing 1300nm light sources for many applications [13–15], there are three problems that need to be considered for operation at 1050nm: (A) chromatic polarization rotation, (B) chromatic dispersion and (C) the relatively high cost of the optical delay line. While the delay line cost is only of economic interest for future commercialization, it is clear that (A) and (B) are detrimental to the main performance indicators for applications in OCT imaging: (1) Output power, (2) axial resolution, (3) relative intensity noise (RIN) and (4) sensitivity roll-off.

In the following we will describe how to overcome problems (A) and (C), which in turn improves the first three performance indicators, leading to high output power, acceptable resolution and low intensity noise. Attempts to overcome chromatic dispersion would very likely improve the last performance indicator, i.e. sensitivity roll-off [40, 41].

Our approach to the presented problems is threefold: First, chromatic polarization rotation is strongly reduced by increasing the diameter of the delay line fiber spool. Second, standard telecom single mode fiber is used in the delay line, reducing cost of the delay line by two orders of magnitude. Third, an additional ytterbium (Yb) amplifier in the FDML laser cavity increases gain and output power considerably.

State of the art semiconductor optical amplifiers (SOAs) in the 1050nm wavelength range exhibit strong polarization dependent gain. It is therefore necessary to manage the polarization of light in the cavity. While fiber-loop polarization controllers allow the adjustment of virtually any polarization state for one wavelength, it is not possible to precisely control the polarization in a broad wavelength range as required in swept-source OCT. Hence, polarization rotation needs to be minimized in the cavity in order to enable a broad laser output spectrum. In an FDML laser, polarization rotation occurs almost exclusively in the passive fiber components, of which the delay line has by far the longest fiber length. Being several hundred meters to kilometers long, the delay fiber is always wound on a compact spool. Birefringence depends on the spool radius R and scales with R^{-2} [42]. We wound the delay line on a 28" bicycle rim (~62cm inner diameter) with a custom

#139343 - $15.00 USD Received 7 Dec 2010; revised 17 Jan 2011; accepted 21 Jan 2011; published 2 Feb 2011
(C) 2011 OSA

built fiber spooling machine, thereby theoretically reducing birefringence in the cavity up to a factor of about $(62/17)^2$=13 compared to common fiber spools with a radius of about 17cm. This ensures stable FDML operation over hours without manual polarization adjustments, which is a significant improvement over previous setups [19, 43].

Until now, all published FDML lasers employed single mode fiber which only supports one transverse mode at the respective operation wavelength [19, 40, 43]. At 1050nm, only specialized fibers such as Corning HI1060 offer true single mode operation. However, these specialized fibers are about two orders of magnitude more expensive than standard single mode fibers (SSMF) such as Corning SMF28 or OFS Allwave ZWP. This made the delay fiber one of the most expensive components in 1050nm FDML lasers, potentially impeding commercialization. SSMF are produced in large scale for the telecommunications industry, resulting in a very low price per meter. Below their cutoff wavelength of around 1280nm, SSMF can support higher transverse modes besides the fundamental mode. Nevertheless, and in contrast to multi mode fibers, which support >>100 modes, only a few modes can propagate around 1050nm [44]. In consequence, and in analogy to oligo-mode operation of bulk lasers [45], we term this type of fiber oligo-mode fiber (OMF). OMF is sometimes also referred to as low-mode-number fiber [46], or few-mode fiber [47]. Fiber modes are eigen-solutions of the characteristic fiber propagation equation. Hence, energy is only transferred between modes at perturbations to the original symmetry and material properties. For our delay line, higher modes would either experience increased damping or reduced overlap with the fundamental mode at the boundary to the next component after the delay line, which needs to have true single mode pigtails for proper functionality. Both effects would simply sum up to higher loss of the delay line. However, we verified experimentally that OMF based delay line (OFS Allwave ZWP) has loss similar to a HI1060 based delay line of same length. Transition loss by mode field mismatch is partially compensated by a lower intrinsic fiber loss of OMF compared to specialized SMF. For instance, Corning specifies a loss of 1.5dB/km for HI1060 compared to ~0.8dB/km intrinsic loss for SMF28. Nevertheless, we further decreased the transition loss by fusion splicing HI1060 pigtails to the OMF delay line. We checked that only the fundamental mode in the OMF part is excited by observing the far field intensity of ~1m SSMF (OFS Allwave) with a CCD camera. Light in the 1050nm range was launched via true single mode fiber (Corning HI1060), both fibers having FC/APC ends.

While loss in the delay fiber itself is not critical, 1050nm fiber components exhibit higher loss and lower gain than their telecommunication wavelength counterparts. Additionally, chromatic dispersion is much stronger, creating additional loss and limiting the output spectrum [43]. In a previous experiment, a tapered amplifier (TA) was inserted into the cavity as an additional gain element apart from an SOA [40]. The system provided better performance than previous setups, but the output power was not as high as expected and the coupling to the TA inserted a free space path in the otherwise compact fiber cavity. Hence, instead of the TA, we employ an ytterbium doped fiber amplifier (YDFA). Approximately 16cm of highly doped fiber (Liekki Yb1200-4/125) provides good amplification bandwidth and inherent safety concerning both laser self damage and patient safety. This length provides enough gain and simultaneously has a limited amount of energy stored as population inversion.

Apart from modifications as described, the cavity layout is similar to previous FDML setups (Fig. 1). In FDML lasers, the cavity length is determined by the sweep speed of the tunable wavelength filter. We drive our fiber Fabry-Perot tunable filter (Lambdaquest, LLC., special “no gel” version) sinusoidally near a mechanical resonance at 171kHz. Subsequently, the so called “buffering” technique of time-multiplexing multiple sweeps to increase the sweep rate was used [48, 49]. The intracavity SOA current was modulated with a fast laser diode driver (Wieserlabs WL-LDC10D). During the time intervals the SOA was switched off, only a limited amount of ASE from the YDFA was observed. Using a 4x or an 8x buffer stage, the sweep rate was increased to 684kHz and 1.37MHz, respectively.

#139343 - $15.00 USD Received 7 Dec 2010; revised 17 Jan 2011; accepted 21 Jan 2011; published 2 Feb 2011
(C) 2011 OSA

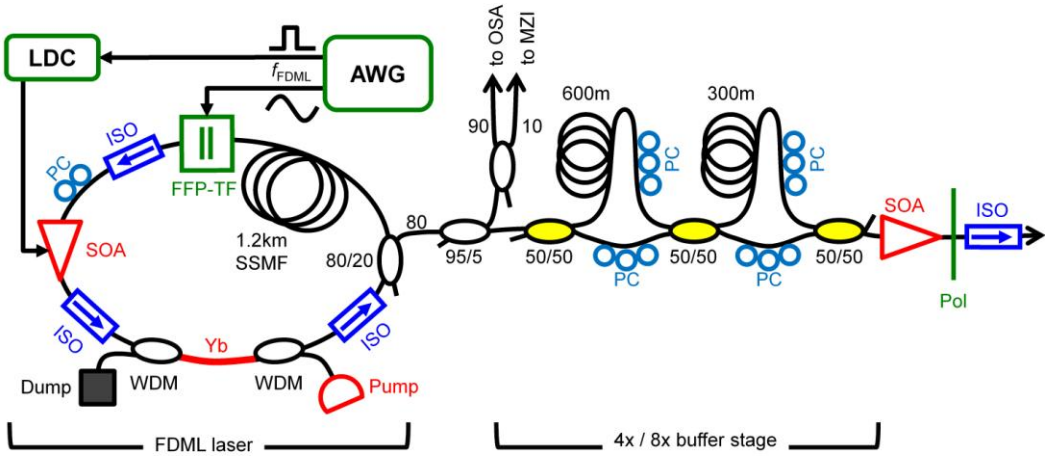


Fig. 1. FDML laser and buffer stage layout. AWG: arbitrary waveform generator; LDC: laser diode controller; FFP-TF: fiber Fabry-Perot tunable filter; ISO: isolator; SOA: semi-conductor optical amplifier; PC: polarization controller; Dump: beam dump; WDM: wavelength division multiplexer; Yb: ytterbium doped fiber; SSMF: standard single mode fiber (OFS Allwave ZWP); Pump: 978nm pump diode; OSA: optical spectrum analyzer; MZI: Mach-Zehnder interferometer; Pol: polarizer.

The buffer factor could be conveniently switched by connecting or disconnecting the last buffer element (not shown in Fig. 1) with FC/APC connectors. Light is coupled out directly after the YDFA to provide the highest possible amount of output power. A high output coupling ratio also decreases the incident power on the following components. At a sweep rate of 684kHz and ~160mW pump diode power, 47mW average power at a sweep range of 80nm was observed directly after the laser output. Since at 684kHz the laser duty cycle is only 25% due to buffering, the instantaneous power for the active sweep reached values of up to several hundred mW in the sweep center. At 1.37MHz sweep rate and a sweep range of 60nm, an output power of 42mW was achieved at ~160mW pump diode power. The filter suffered mechanical damage when we tried to increase the sweep range further. To ensure a long filter lifetime and for various reasons that will be explained in the following sections, we limited the sweep range to 72nm (684kHz) and 43nm (1.37MHz) for characterization and imaging with another filter of the same type (Fig. 2). Apart from the sweep range, the performance was similar to that with the first filter.

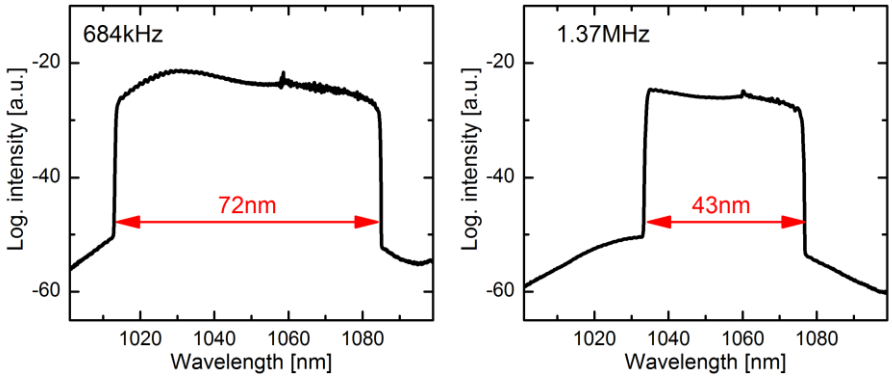


Fig. 2. Output spectra directly after the laser cavity for 684kHz and 1.37MHz sweep rates.

#139343 - $15.00 USD Received 7 Dec 2010; revised 17 Jan 2011; accepted 21 Jan 2011; published 2 Feb 2011
(C) 2011 OSA

2.2. Spectral shaping

For OCT imaging, the respective output powers and spectral shapes of each buffered sweep should be equal. If this is not the case, the different brightness of adjacent axial scans leads to stripe-pattern artifacts in the B-frames and in the *en face* visualizations of the recorded data set. Taking into account the chromatic dependence of the coupler splitting ratios, it is straightforward to show that equal powers and shapes are not possible with buffer stages that have a higher multiplexing factor than two. Therefore, we use an additional "booster" SOA after the buffer stage. The SOA current is controlled via a Labview program which enables precise control of the spectral shape of each buffered sweep.

Previous research in spectral shaping for OCT focused mainly on axial resolution [50], which sometimes leads to spectral shapes that produce strong side lobes in the axial point spread function (PSF) of the OCT image [51]. It is sometimes claimed that a Gaussian spectrum is ideal for OCT imaging since it does not produce side lobes [52], and spectral shaping has often been carried out with a target Gaussian spectrum [28]. However, since an exact Gaussian shape has by definition power contributions from zero to infinite wavelengths, it is not possible to generate a true Gaussian spectrum in real world experiments. Thus, the Gaussian spectra are cropped and sidelobes are generated. In fact, (approximate) Gaussian fringe envelopes do not have a good ratio of side lobe suppression to resolution compared to other known envelopes [53]. Side lobe suppression, side lobe roll-off and full width at half maximum should be well balanced by an optimized, often non-Gaussian, fringe envelope [14, 54].

Apart from these PSF related considerations, spectral shaping also has an impact on system sensitivity, if the absorption in the sample or on the way to the sample is taken into account. For instance, the spectral dependence of water absorption in the 1050nm wavelength range reduces the number of backscattered photons from the retina with increasing distance from the absorption minimum at around 1060nm. For the presented ultrahigh imaging speeds of up to 1.37MHz, we employed a Hann shape as compromise between axial resolution and sensitivity. The Hann shape has a rather steep edge, which means that most of the optical power is located in the center of the wavelength sweep. In our case, this center is at about 1050nm, which concentrates power near the water absorption minimum [55]. Hence image penetration is enhanced compared to the unshaped spectrum. Spectral shaping was performed by iteratively changing the transient current of the booster SOA after the buffer stage [56]. The required change in the SOA drive current after each shaping step was determined by the difference between the reference arm spectrum of the OCT setup and the target shape. For spectral shaping, we did neither take into account the exact shape of water absorption nor the time-wavelength nonlinearity of the source. Both effects are small for our spectral shape and the high buffering ratios. Due to the steep wings of the Hann shape, only a small amount of power would be transferred from center to outer parts of the spectrum. With 4x and 8x buffering, the time-wavelength dependence is also already close to linear.

2.3. Swept source characterization

Figure 3 (left) shows fringes generated with an additional recalibration arm in the OCT interferometer (see section 3.1 and Fig. 4) and sensitivity roll-offs acquired with a motorized Mach-Zehnder interferometer for both 684kHz (top) and 1.37MHz (bottom). The fringe envelopes of all 4 or 8 buffered sweeps are very similar, which is a consequence of spectral shaping with a Hann target shape *after* the buffer stage, as discussed in the previous section. The coherence properties are only slightly affected by loss in the buffer stage and the subsequent amplification in the booster SOA. Thus all buffered sweeps show similar sensitivity roll-off. Figure 3 (right) shows the sensitivity roll-offs recorded with a 5GS/s 8 bit oscilloscope over almost the entire range for retinal imaging. Interestingly, the sensitivity roll-off at 684kHz is comparable to the one at 1.37MHz, despite a 2x higher buffering factor. This is due to the fact that the coherence is largest in the center of the sweep, which is resonant to the cavity round trip time.

#139343 - $15.00 USD Received 7 Dec 2010; revised 17 Jan 2011; accepted 21 Jan 2011; published 2 Feb 2011
(C) 2011 OSA

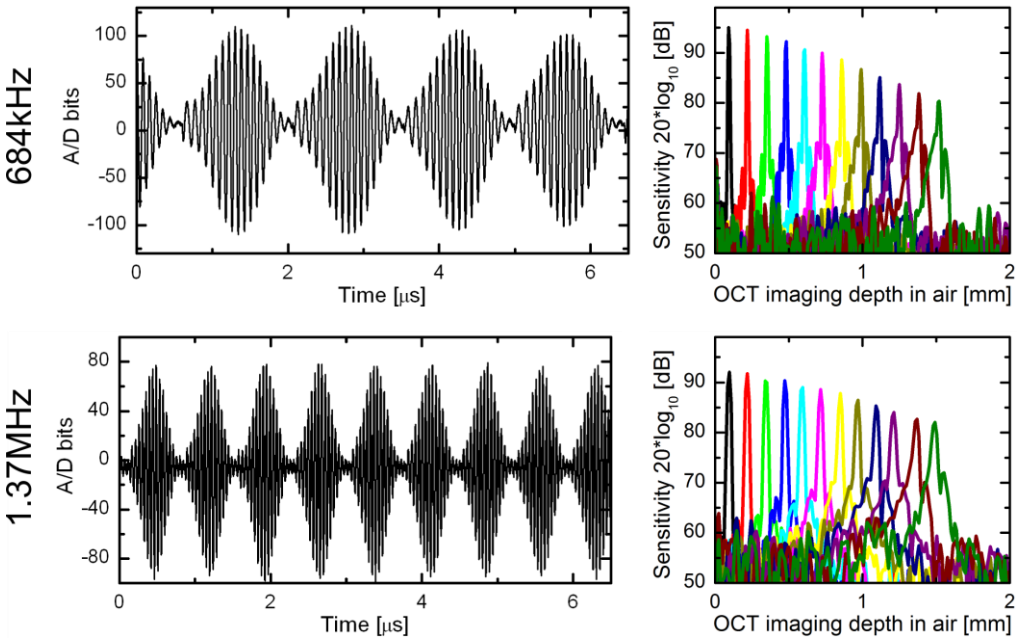


Fig. 3. Hann shaped fringes and sensitivity roll-off for both 684kHz (upper row) and 1.37MHz (lower row). A linear fit to the PSF decay over the first millimeter imaging range yields R-number values of 0.12mm/dB (684kHz) and 0.15mm/dB (1.37MHz).

Away from the center, dispersion in the intracavity delay line deteriorates coherence properties [41]. At 1.37MHz, the sweep range is considerably smaller than at 684kHz, which balances the effect of larger filter mismatch. The varying coherence over the sweep does also produce a varying spectral shape when the interferometer delay is increased: The fringe contrast in the low coherence parts of the sweep decays more rapidly than in the parts with larger coherence, thus producing distorted, asymmetric spectral shapes. Hence the axial resolution deteriorates for larger delays and side-lobes in the PSF build up. A linear fit to the first millimeter imaging range yields R-numbers [41] of around 0.14mm/dB, which is comparable to line-scan camera based SD-OCT systems operating at less than a fourth of the axial scan rate [31]. Sensitivity roll-off performance of this magnitude has been shown to significantly compromise image quality at increasing depths within the imaging range [32]. Some commercially available short-cavity swept lasers do have narrower instantaneous linewidths, enabling very little loss of signal over long imaging ranges. R-number values of ~0.6mm/dB have been demonstrated at 100,000-200,000 axial scans per second [32], approaching the 1.4mm/dB FDML performance with a dispersion managed delay line as shown in [41]. However, it is still unclear if axial scan rates of more than 1MHz as presented in this paper are feasible with short cavity designs maintaining such good coherence, considering the fundamental limits to sweep speed and mode spacing in short cavities [13].

The axial resolution in air has been determined to be 16μm at 684kHz and 25μm at 1.37MHz. Assuming a refractive index of 1.35, the theoretical axial resolution in tissue is 12μm and 19μm, respectively. The relative intensity noise (RIN) varies over the sweep. RIN decreases towards the wavelength for which the FDML criterion is fulfilled. Interestingly, a slight peak in RIN is observed in the vicinity of this wavelength. The booster amplifier is saturated by the high power incident from the FDML cavity, thus reducing RIN by a factor of about 4 compared to RIN directly at the output of the cavity. The average RIN values from DC to the detector bandwidth of 350MHz are 1% for 684kHz and 1.5% for 1.37MHz. For both sweep rates, minimum and maximum RIN values are about 0.5% and 3%, respectively. It should be emphasized that the higher values here compared to the ones in [41] can be attributed in part to the 3.5 times higher electronic bandwidth.

#139343 - $15.00 USD Received 7 Dec 2010; revised 17 Jan 2011; accepted 21 Jan 2011; published 2 Feb 2011
(C) 2011 OSA

3. OCT Setup, data acquisition and processing

3.1. OCT interferometer design

Many SS-OCT systems at 1050nm are more than 3dB away from shot noise limited detection [21, 23, 43]. For ultrahigh speed imaging, this eventually limits the axial scan rates. For retinal imaging, sensitivity values of more than 90dB are preferable for good image quality. Under this criterion, SD-OCT line rate seems to be limited to around 300kHz with currently available line scan cameras [31]. In high speed SS-OCT, especially with 1050nm lasers, it is essential to use dual balanced detectors to achieve shot noise limited sensitivity [57], because the high fringe frequencies require high speed photo receivers which have lower transimpendance gain. Therefore the power level in the reference arm has to be increased. Unfortunately, the non-flat spectral response of beam splitters in the interferometer leads to a deterioration of signal-to-noise ratio [58, 59]. We present a completely symmetric configuration that compensates for the spectral dependence of the coupling ratio at a cost of 3dB in sensitivity (Fig. 4). Since the spectral response of the fiber couplers is very reproducible, a suitable arrangement of two couplers can have an essentially flat spectral response at one of the two final output ports. By proper combination of all the coupler ports in our interferometer, the spectral shape of the incident reference arm signal is very similar at the two dual balanced detector inputs, which increases common mode noise rejection considerably. This avoids the need for separate digitization of two unbalanced detectors [60]. The latter is currently impractical for ultrahigh speed systems, which come to the limits of currently feasible data rates. Moreover, our design creates additional access points to the interferometer: We implemented an additional recalibration arm for time to optical frequency resampling and a free coupler port which was used to monitor the reference arm power.

Taking into account the 3dB penalty, shot noise limited performance is achieved. We measured a system sensitivity of ~95dB for the 684kHz configuration and ~92dB for the 1.37MHz configuration with 1.5mW power on the sample. Accounting for a 65% free-space to fiber coupling efficiency in our setup, 3dB spectrally balanced interferometer penalty, and 0.7A/W detector responsivity (Thorlabs PDB130C, 350MHz analog bandwidth), the measured sensitivity corresponds to the theoretical shot-noise limit of 100dB and 97dB, respectively [8]. We verified that sensitivity stays constant within measurement accuracy for reference arm powers incident on the photo detector ranging from at least 120µW to 180µW, which is another indication for shot noise limited detection [61]. Due to the symmetric interferometer design, the low frequency background in the dual balanced signal was less than 2% of the unbalanced value, with most of the balanced signal having a higher suppression ratio. Interestingly, we observed slight polarization dependence of the remaining DC component, which we attribute to polarization dependence in the splitting ratio of the fiber couplers.

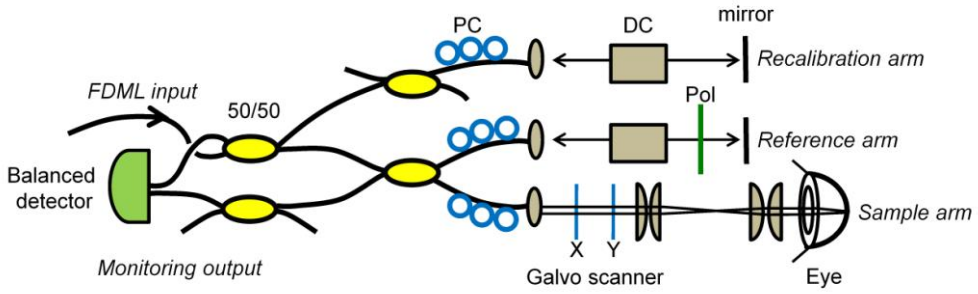


Fig. 4. Layout of the symmetric Michelson interferometer. PC: polarization controller; DC: dispersion compensation for sample arm lenses; Pol: polarizer. All fiber couplers have a 50/50 splitting ratio.

#139343 - $15.00 USD Received 7 Dec 2010; revised 17 Jan 2011; accepted 21 Jan 2011; published 2 Feb 2011
(C) 2011 OSA

To enable retinal imaging over an ultrawide-field of view, we used two inch diameter optics for the relay telescope. As indicated schematically in Fig. 4, a doublet similar to a Plössl eyepiece design was used as both first and last element. However, we used stock plano-convex spherical lenses instead of achromats. This design is achromatic enough for the limited wavelength range used, and seemed to deliver slightly better performance than the available stock achromats. Focal lengths of the lenses were 2x150mm for the front lenses and 2x75mm for the lenses facing the eye. We discarded a Volk 60D ophthalmic lens as last element, which gave even a wider field of view at the cost of reduced image quality, which is maybe due to the inappropriate antireflection coating around 1050nm.

3.2. Electronics, sampling and recalibration

Data acquisition at both 684kHz and 1.37MHz axial scan rate was performed with a 12 bit, 400MS/s data acquisition card (CompuScope CS12400, Gage Applied Technologies). Hence 584 samples were acquired per A-scan at 684kHz, and only 292 samples at 1.37MHz. Due to the strong common mode noise rejection in our symmetric detection scheme, aliasing of high frequency noise from the 350MHz bandwidth photo detector was not perceptible. Nevertheless, a 270MHz low pass filter (Minicircuits BLP-300+) was used to approximately ensure Nyquist sampling without damping of high frequency interference signals. Apart from common mode noise rejection, our detection scheme also makes efficient use of the analog-to-digital (A/D) range by sacrificing less than 2bits to the remaining background. While this can also be achieved with an AC coupled detector or a high pass filter, both solutions make the OCT imaging range near zero delay inaccessible.

Since the intracavity filter was driven sinusoidally, we performed numerical recalibration of the raw fringe data to achieve equal sample spacing in optical frequency. The additional recalibration arm in the interferometer provided the necessary signal without the need for a separate Mach-Zehnder or inconvenient insertion of a mirror in the sample arm. Each buffered sweep was recalibrated separately to account for nonlinearities in the sweep caused by the different lengths of the delay fibers, resulting in 4 different calibrations at 684kHz and 8 different calibrations at 1.37MHz. Recalibration was performed prior to imaging and no sweep-to-sweep variations in the time-frequency characteristics were found, eliminating the need to record a separate recalibration for each A-scan in a data set. For proper resampling, it is beneficial to sample the raw data beyond the Nyquist limit. With the available 400MS/s detector card, this criterion was not fulfilled over the entire imaging range, especially at 1.37MHz. To reduce signal wash-out at larger delays, the OCT raw data was sinc-interpolated prior to resampling [62]. Additional dispersion compensation was carried out numerically [63].

3.3. Bidirectional scanning and removal of "zipper" artifacts

In ultrahigh speed OCT imaging, non resonant galvanometer scanners are stressed to their mechanical limits. Most OCT systems typically employ linear ramps for the fast galvanometer axis. During fly back time, image data is discarded. As imaging speed increases, the relative fly back time has to be extended due to the limited response of the scanner. In other words, the short duty cycle in which image data is acquired eventually severely decreases the effective OCT imaging speed. Thus, the effective imaging speed is lower than the actual axial scan rates. A solution to the problem is to employ bidirectional scanning protocols for the fast axis, where only a small region around the turning point has to be discarded [14]. For high speeds, sinusoidal waveforms enable the highest scan speeds. Due to imperfections in the driving electronics and off-axis vibrations of the mirror, the beam follows different trajectories during forward and backward motion. This results in "zipper" like artifacts in en-face views of the acquired OCT data sets.

Numerical post-processing is a feasible way to eliminate these artifacts. Here, we present two main improvements to the recalibration procedure presented in [14]. First, the film stripe pattern was replaced with an equally spaced wire grid, which generates bright and background free OCT signals. A 3D data set of the grid is acquired and processed as in [14],

#139343 - $15.00 USD Received 7 Dec 2010; revised 17 Jan 2011; accepted 21 Jan 2011; published 2 Feb 2011
(C) 2011 OSA

resulting in a 5th or 7th order interpolating polynomial for odd and even frames, valid over the entire data set. This polynomial does however not yet describe the galvanometer motion perfectly, and slight zipper artifacts remain. A main reason for this lies in the non-uniformity of the wire grid, which was not equidistant up to the required precision. We therefore employ a second fine tuning step: Offset values are specified at five points equally distributed over the B-scan. Subsequently, offsets values for the entire B-scan are computed by a cubic Hermite interpolation between these points. These offsets are finally added to the original interpolation curve based on the polynomial. The magnitude of the offsets can be controlled interactively in an en-face view of the full data set under consideration. The complete resampling curve remains valid during at least one imaging session, if scan parameters are not changed. We checked that the same interpolation is valid for retinal OCT imaging data sets of several different eyes, which were obtained during one afternoon at 684kHz. Nevertheless, offsets may need fine adjustments on a day to day basis, using the same underlying polynomial. At 1.37Mhz, the galvanometer scanner motion needs to be corrected separately for each data set. The determination of these adjustments might be facilitated by the fact that there is one unique set of offset coefficients for which zipper artifacts disappear. This suggests that offset values might be automatically computed by the help of a suitable en-face image sharpness metric or by cross-correlating even and odd frames. Thus the wire grid needs to be imaged only once for each scanner setting.

For retinal imaging with 1900 axial scans per B-frame, we used 86.5% of the total scan duty cycle for imaging at both 684kHz and 1.37MHz. No data was acquired in a symmetric region around the turning points of the sinusoidal driving waveform, lowering effective acquisition rates to 592kHz and 1.19MHz. The resulting effective sustained frame rates over the entire 1900x1900xN 3D data set for 1900 lines per OCT B-scan are 309 frames/second and 612 frames/second, respectively.

4. Retinal imaging

4.1. Beam delivery design considerations

As discussed in the introduction, one important driving factor in the development of high-speed OCT systems is the desire to obtain large, densely sampled 3D volumes within reasonable acquisition times. In retinal imaging, acquisition times should fall below a few seconds. Otherwise, eye motion would lead to distortions in parts of the data set. This does severely limit the fundus area that can be densely sampled even for current experimental ultrahigh speed systems [18]. For dense sampling, the necessary number of axial scans per fundus area depends on the transverse spot size of the scanning beam. Albeit ultrahigh transverse resolution can be achieved with adaptive optics OCT systems, the extracted en-face fundus views are restricted to very limited field of views of less than 2° [18]. With standard optics, the transverse resolution depends on beam diameter on the pupil. Due to optical aberrations of the scanning optics, the scanning beam shifts on the pupil for large viewing angles. We thus chose a beam diameter of 1.1mm ($1/e^2$ intensity), which yields a theoretical spot size of 27µm ($1/e^2$ intensity) on the retina. The system's scanning optics limited the field of view to 70°x70° in case of a non-mydriatic eye, because it was not possible to achieve a perfect pivot point in the center of the iris over the full scan angle. With 288µm image size per degree of external viewing angle, this results in an OCT volume consisting of 1900x1900 isotropically sampled axial scans. The sampling points have a spacing of 10.6µm on the retina. If we now assume that at least two sampling points per theoretical spot size (27µm) are required, our sampling density is sufficient to assure complete gap free coverage of all resolvable features in the imaged volume. Hence, no information is missed, and cross-sectional images can be extracted along arbitrary coordinates *after* data acquisition, as will be demonstrated in the next paragraph. The assumption of at least 2 sampling points per theoretical spot size seems reasonable, considering optical aberrations by both beam delivery optics and the eye itself. Moreover, a thorough investigation of the system's transverse resolution should not only be based on the single

#139343 - $15.00 USD Received 7 Dec 2010; revised 17 Jan 2011; accepted 21 Jan 2011; published 2 Feb 2011
(C) 2011 OSA

parameter given by spot size [64]. There are multiple different definitions of resolution, and aspects such as confocal gating, the real shape of the transverse point spread function as well as the system's signal to noise ratio have to be taken into account [64]. Accordingly, the required amount of oversampling is debatable, and may even vary over the imaged volume.

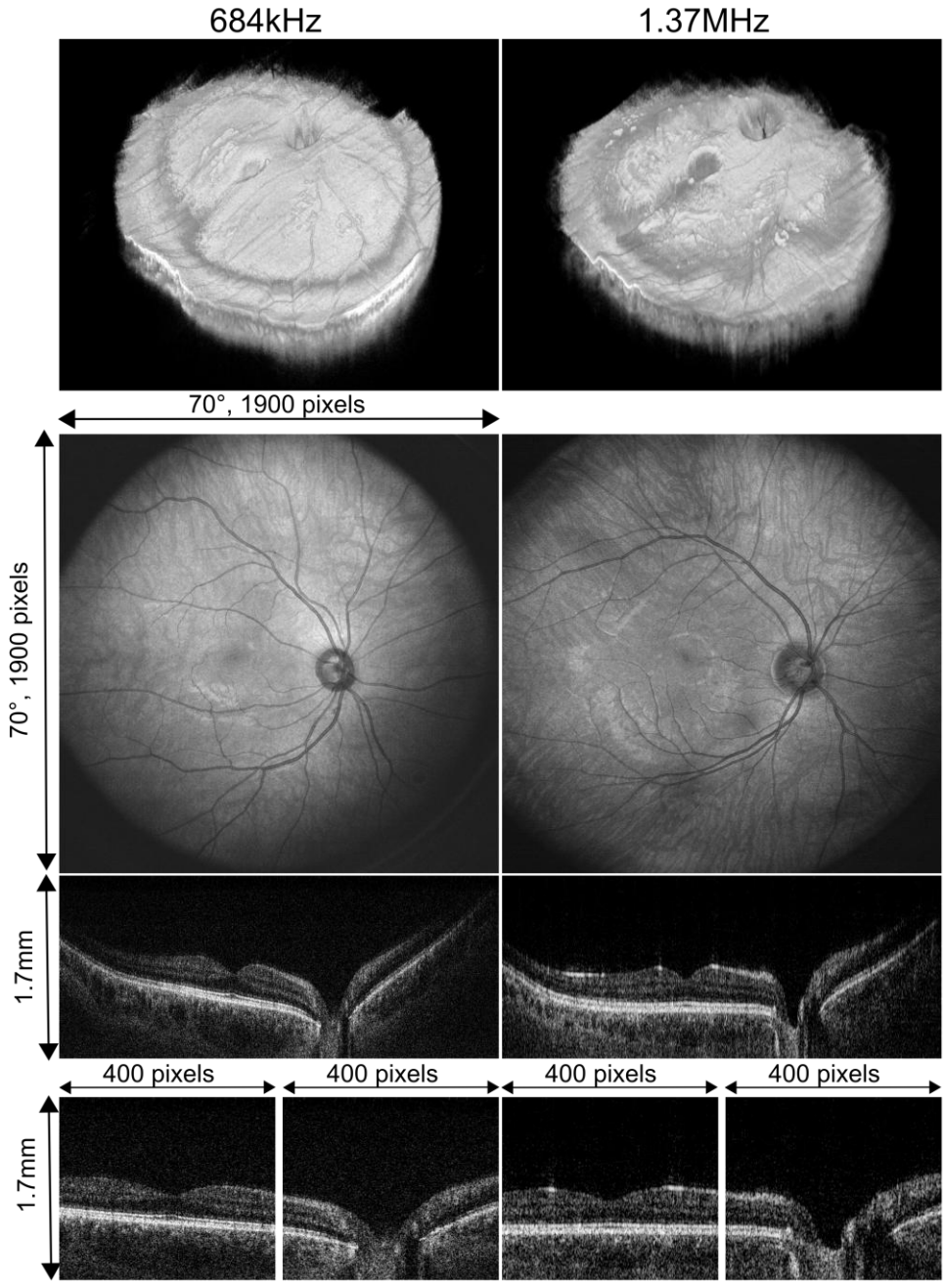


Fig. 5. Densely sampled 3D data sets consisting of 1900x1900 axial scans. Top: 3D rendering of the whole data set. Middle: reconstructed fundus view. Penultimate row: OCT cross-sectional images through both macula and optics disc, covering the full imaging range of the system of ~1.7mm in tissue (assuming n=1.35). Bottom row: Enlarged images of macula and optical nerve head. The OCT zero delay is located at the bottom of the B-frames.

#139343 - $15.00 USD Received 7 Dec 2010; revised 17 Jan 2011; accepted 21 Jan 2011; published 2 Feb 2011
(C) 2011 OSA

The 2.5x oversampling applied seems to be a reasonable choice to produce four megapixel en-face images similar to SLO fundus views. The ~70° field of view, almost 4 times larger in area than previously demonstrated, facilitates inter-modality investigations. The large 1900x1900 A-scan data sets almost fill the 4GB available internal memory of the data acquisition card at 684kHz. Including the galvanometer scanner dead times, these data sets were acquired in 6.1s (684kHz) and 3.0 seconds (1.37MHz). This illustrates that for such large data sets, more than 700kHz axial scan rate should be available, since clinical application above 3s-5s acquisition time is impaired [18]. Taking into account that high-speed microsacades may occur during data acquisition [65], even multi-megahertz axial scan rates would be necessary.

4.2. Imaging results: 3D data sets and 2D projections along arbitrary coordinates

In the following, we will present one densely sampled data set for imaging at 684kHz and one data set at 1.37MHz from two different individuals. Both data sets have ~70° field of view and consist of 1900x1900 axial scans. Due to removal of zipper-artifacts as discussed in section 3.3., the actual resolution of the resulting images is about 5% lower in the horizontal (*x*-) direction. Power on the eye was 1.5mW for both data sets. This power level is consistent with safe ocular exposure limits set by the American National Standards Institute (ANSI) [66], and written consent of the subjects was obtained before performing experiments. Figure 5 depicts a 3D rendering of the whole volume, a fundus reconstruction and one B-frame of each data set with enlarged parts showing both macula and optic disc. The B-frames show good signal to noise ratio, separation of intra-retinal layers and penetration through the choroid. As expected, the axial resolution is significantly lower at 1.37MHz than at 684kHz, whereas image penetration is similar, despite sensitivity loss due to the higher axial scan rate. Both effects are due to the narrower laser sweep spectrum at 1.37MHz, which, on the one hand decreases the axial resolution, but on the other hand is less affected by water absorption as discussed in the section on spectral shaping.

The single B-frames do also indicate several of the problems encountered at these high imaging speeds. Both B-frames in Fig. 5 show the full imaging range of the system, limited by the sampling rate of the A/D card. Due to aberrations of the beam delivery optics and intrinsic curvature of the fundus, the whole imaging range is just large enough to contain the axial elongation of the fundus. Again, the relatively small sweep spectrum at 1.37MHz helps to reduce the fringe frequency such that the imaging range remains comparable to 684kHz. Data was acquired with the choroid close to zero delay of the interferometer, because higher sensitivity near zero delay compensates partially for signal loss in deeper layers. At 1.37MHz, the choroid was slightly closer to zero delay, and the contrast of the choroidal vessels in the full fundus reconstruction is consequently increased compared to 684kHz. Both 3D renderings and the single B-frames show that signal from fundus layers above the retinal pigment epithelium (RPE) decreases towards the edges of the transverse imaging range. Best OCT image quality is achieved in the central 50° to 60° of the whole field of view. We believe that three main reasons for this behavior are sensitivity roll-off and related axial PSF broadening, incident angle on the retina and aberrations of the beam delivery optics. The influence of sensitivity roll-off on the image quality can best be seen in the unflattened B-frames in Fig. 5: The outer parts of the image are located at the end of the imaging range, with corresponding impact of sensitivity roll-off. Note that for OCT imaging, a much lower sampling rate of 400MS/s was used compared to roll-off measurement with 5GS/s as described above. Distance from OCT zero delay is influenced by the beam delivery optics. Thus an optimized design may flatten image curvature and outer parts of the retina would come closer to zero delay, reducing the impact of sensitivity roll-off.

To enable advanced sectioning of the data sets, both motion correction and reduction of fundus curvature were carried out in post-processing by flattening with respect to the RPE. Due to lower signal strength at the edges of the field of view and steep features around the RPE, flattening was complicated and some curvature remained. The following figures and movies all show data from these flattened data sets.

#139343 - $15.00 USD Received 7 Dec 2010; revised 17 Jan 2011; accepted 21 Jan 2011; published 2 Feb 2011
(C) 2011 OSA

To improve image quality, averaging is performed in many OCT systems. Averaging has two main goals: higher signal to noise ratio (SNR) and speckle reduction. Usually, several B-scans acquired “at the same location” are averaged. While averaged B-scans from exactly the same volume yield higher SNR, one has to take into account that the speckle pattern is stationary.

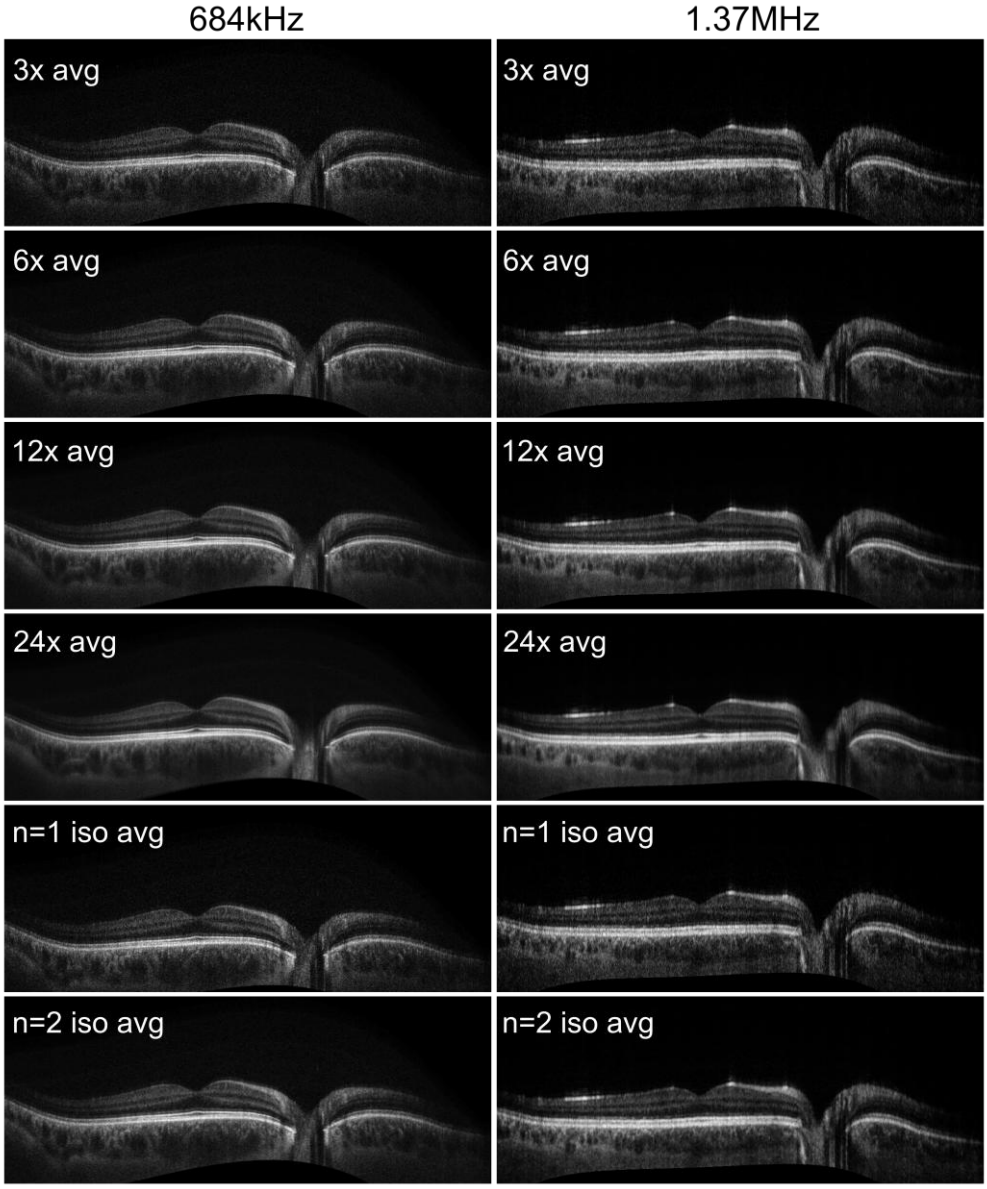


Fig. 6. Comparison of different averaging modalities at the same position as the B-frames in Fig. 5. Top four rows: Averaging of 3, 6, 12 and 24 B-frames along the slow scan axis. Left column: 684kHz (Media 1, Media 2, Media 3, Media 4). Right column: 1.37MHz (Media 5, Media 6, Media 7, Media 8). Bottom: Isotropic averaging of order n=1 (684kHz: Media 9; 1.37MHz: Media 10) and n=2 (684kHz: Media 11; 1.37MHz: Media 12). For instance, order 1 isotropic averaging means that for each pixel all laterally surrounding voxels are averaged, resulting in a total number of 9 averaged voxels per output pixel. Movies show fly-throughs of the complete data sets. The data sets were flattened prior to averaging (see text).

#139343 - $15.00 USD Received 7 Dec 2010; revised 17 Jan 2011; accepted 21 Jan 2011; published 2 Feb 2011
(C) 2011 OSA

Thus speckle reduction can only be achieved when the averaged scans are slightly displaced from each other. In practice, OCT systems such as the Heidelberg Spectralis benefit from imperfect sample tracking or sample motion to achieve speckle reduction. For this reason the extent of the averaged volume is not precisely defined. Dense sampling enables precise control over the averaging pattern after data acquisition. Thus the optimum amount of averaging before feature wash-out occurs can be determined in post-processing for each sample individually. In the following, we compare two averaging protocols.

First, we perform averaging of B-frames along the slow axis, which is similar to the usual averaging of multiple scans from the same location. The images in the top rows of Fig. 6 show a series of 3x to 24x averaged frames. It can be clearly seen that signal to noise ratio is increased while speckle is decreased, leading to a smoother appearance of the image. Image penetration is limited by the sample rate of the A/D card. The quality of the images compares well with standard OCT images acquired at lower speed. Hence reduced sensitivity caused by the high speed is compensated by averaging. However, with increasing number of averaged slices, resolution is decreased non-isotropically in the direction of averaging. For instance, the 24x averaged frames show wash out of features at the optic disc.

Due to lateral oversampling of the data sets, we were able to apply a new averaging protocol: isotropic averaging, in which the intensity of each pixel in a cross-sectional image is determined by the average with its laterally surrounding voxels. This way $(2n + 1)^2$ pixels are averaged for isotropic averaging of order n. Figure 6 (bottom) shows isotropic averaging of order 1 and 2. For instance, for order n=1, 9 adjacent voxels from the volume at equal axial depth are averaged, however only from 3 different B-frames. Thus, resolution loss should be similar in all lateral directions due to isotropic sampling. Contrary to B-frame averaging, iso-

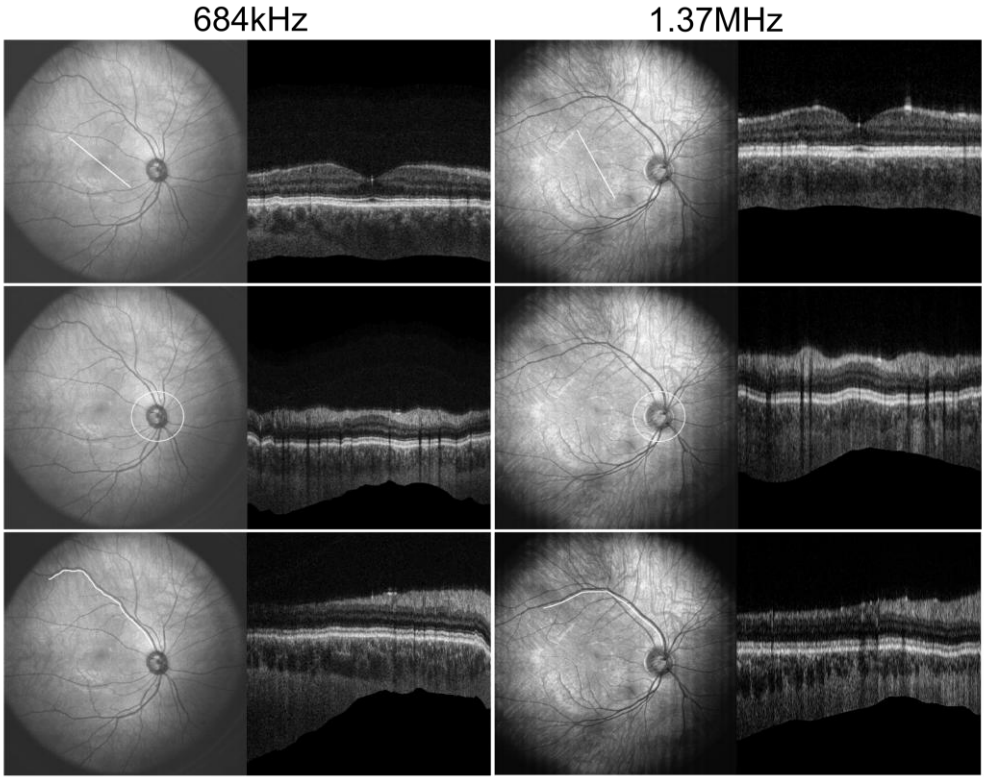


Fig. 7. Sectioning along arbitrary dimensions with isotropically (n=1) averaged data. Top: Rotary scan around the center of the fovea (Media 13, Media 14). Middle: Inflating circumpapillary scan (Media 15, Media 16). Bottom: Arbitrary scan along a mayor blood vessel, showing smaller outgoing vessels.

#139343 - $15.00 USD Received 7 Dec 2010; revised 17 Jan 2011; accepted 21 Jan 2011; published 2 Feb 2011
(C) 2011 OSA

tropic averaging also averages the voxels in the image plane, resulting in non-uniform speckle size, which adds to the impression of more speckle noise. Hence the frame averaged images appear smoother but may exhibit less detail.

Fly-through movies of the full data sets allow for a quick evaluation of the different averaging procedures (see media in Fig. 6). The 3x B-frames averaging preserves all features due to oversampling, with higher signal to noise ratio compared to single frames. Speckle noise is more strongly reduced with 6x B-frame averaging, and image blurring is only slightly perceptible.

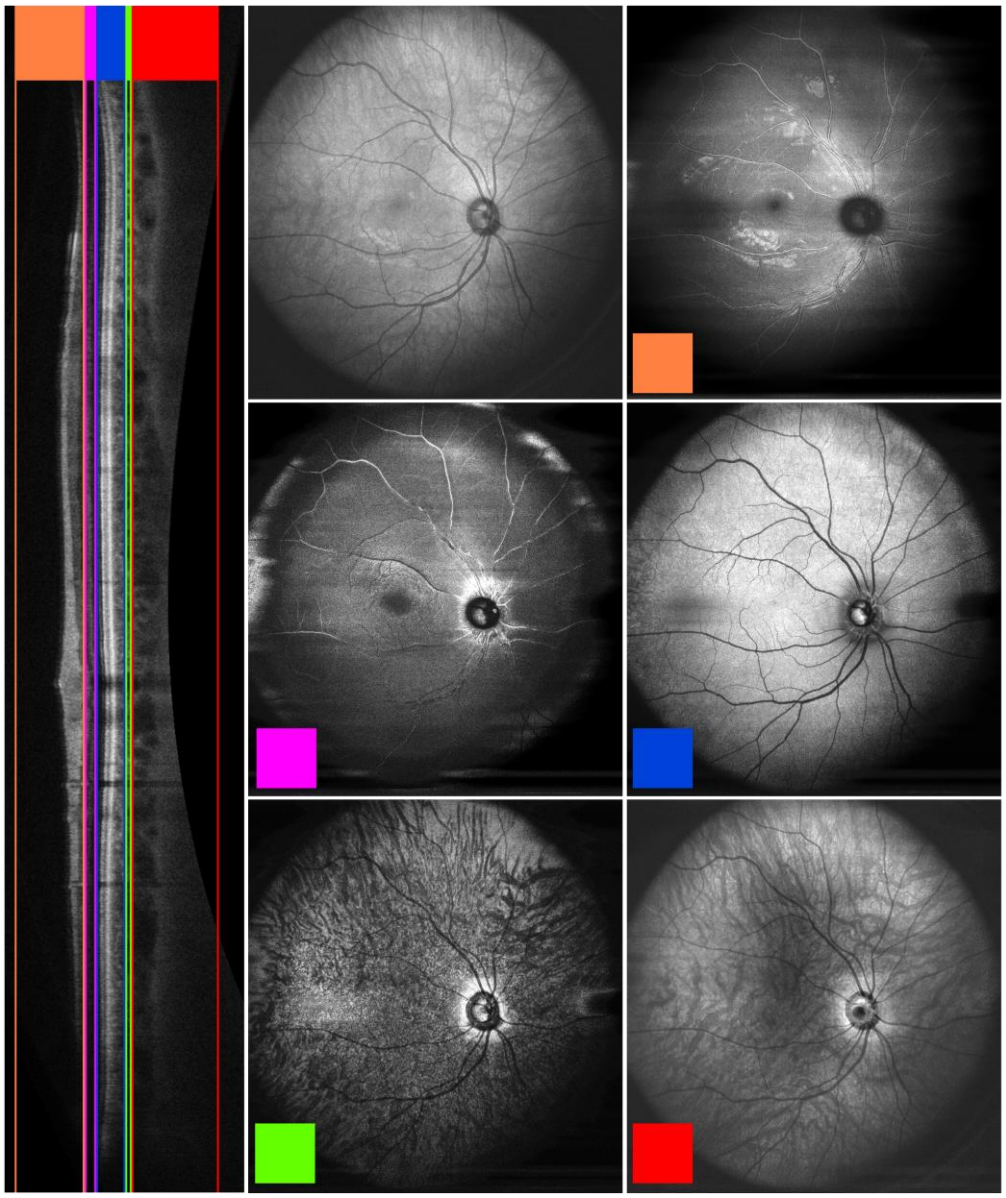


Fig. 8. The densely sampled (1900x1900) OCT volume enables reconstruction of depth-resolved fundus images (684kHz). Corresponding depth locations of the fundus images are color coded in the averaged B-frame on the left. The complete fundus image (integrated along the full depth) in the top left is inserted for comparison and is the same as in Fig. 5. Local shadows and highlights are artifacts from imperfect flattening of the data sets.

#139343 - $15.00 USD Received 7 Dec 2010; revised 17 Jan 2011; accepted 21 Jan 2011; published 2 Feb 2011
(C) 2011 OSA

For 12x and 24x B-frame averaging, the combination of both speckle noise reduction and increased signal to noise ratio allows for clear identification of vessels in the sclera, which are not identifiable in unaveraged B-frames. However, 24x B-frame averaging yields clearly visible blurring, which is especially observable for vessels crossing the slow scan axis at small angles. As expected, isotropic averaging shows less blurring of features that change along the fly-through direction than B-frame averaging for similar numbers of averaged pixels. On the other hand, the images appear more granular. Averaging based speckle reduction relies on a change in sample structure, which necessarily leads to blurring. While isotropic averaging exhibits less speckle noise reduction than B-frame averaging, increase in signal-to-noise ratio is clearly perceptible with only a small amount of blurring.

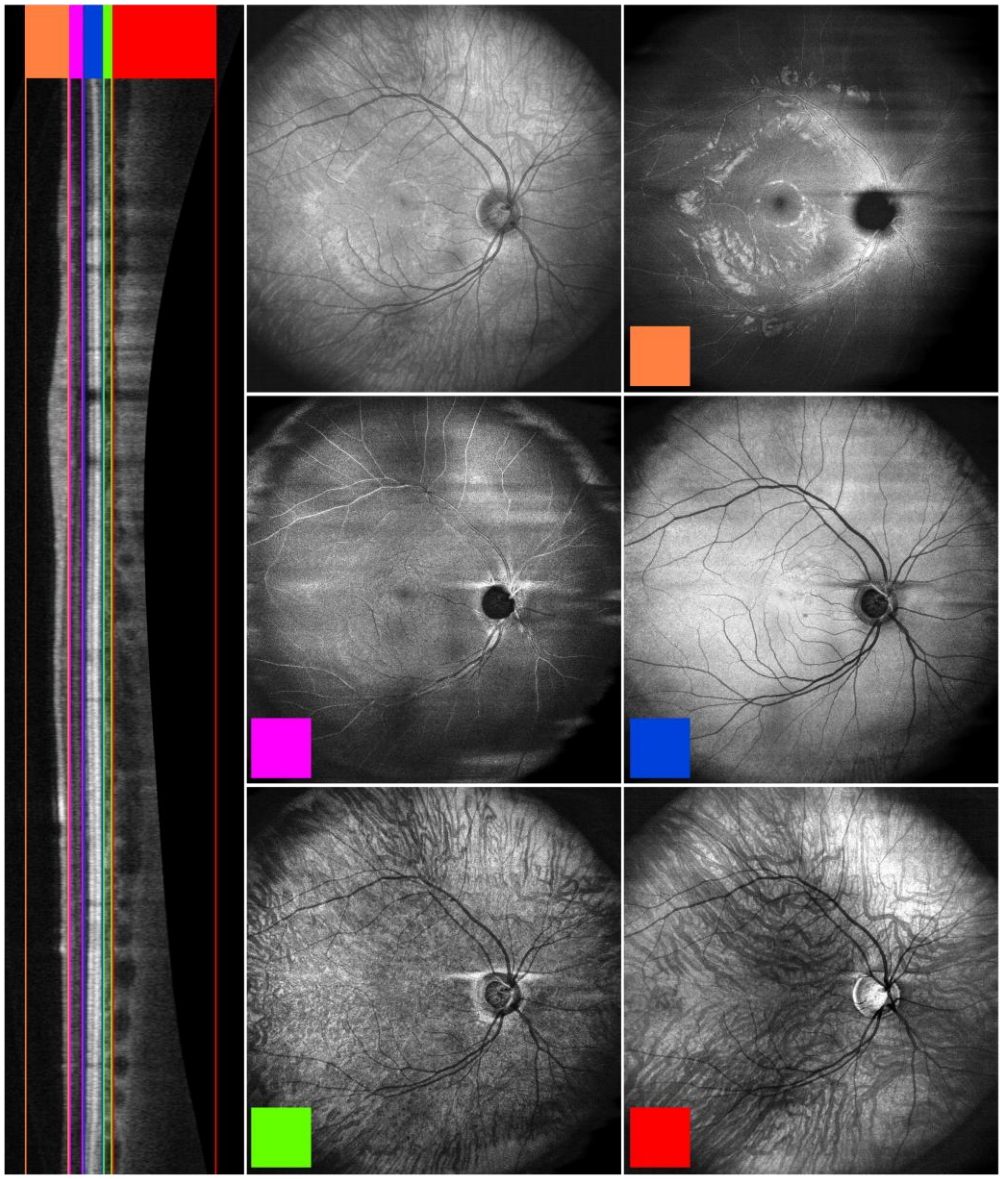


Fig. 9. At 1.37 MHz, reconstructed fundus images are similar in quality to 684kHz.

#139343 - $15.00 USD Received 7 Dec 2010; revised 17 Jan 2011; accepted 21 Jan 2011; published 2 Feb 2011
(C) 2011 OSA

Apart from averaging, the densely sampled data sets also enable reconstruction of cross-sections along arbitrary coordinates *after* data acquisition. This constitutes a significant advantage over lower speed systems, where the desired scan area has to be selected *prior* to data acquisition. Time and hence number of data set acquisitions are usually restricted in clinical environments, and there might be a significant delay between data acquisition and detailed analysis by a physician. Thus, it might be that not all desired information is available when a smaller data set is acquired. Figure 7 (top) depicts a rotary scan around the macula, and Fig. 7 (middle) shows a circumpapilary scan with increasing diameter. In the latter, outgoing blood vessels can be followed over a large area. The corresponding movies show that image quality remains constant, as expected from isotropic sampling. Additionally, cross-section reconstruction is not only limited to such geometrically simple shapes, but it is also possible to reconstruct image data along completely arbitrary coordinates. For instance, we show a virtual scan along a major blood vessel in Fig. 7 (bottom). Such scans may be of clinical value if Doppler functionality is added to integrate or sum the total blood flow in blood vessels. Several outgoing vessels are clearly visible, which might facilitate diagnosis of vessel occlusion or similar pathologies.

In addition to arbitrary reconstructions of cross sections along the axial direction, we also computed depth-resolved fundus images at distinct axial locations, similar to what has been shown in [24, 38]. Figure 8 and Fig. 9 show the fundus slices together with an averaged and flattened B-frame indicating the axial positions. From top to bottom along the axial direction, one can partly identify fiber bundles in the nerve fiber layer around the macula. Next, one can clearly identify vessels in the ganglion cell layer, strong contrast for retinal vessels by shadows and fine structure around RPE and choriocapillaris, and increasing vessel size from regions around Sattler's layer to regions around Haller's layers. It has already been shown by Gorczynska et. al. that these projected fundus images may facilitate rapid interpretation of large 3D data sets in clinical applications [38].

5. Conclusion

In this paper, we demonstrated ultrahigh speed OCT over a ~70° field of view, enabled by a novel 1050nm FDML laser, using an YDFA as second gain element. An achromatic interferometer design is presented, enabling shot noise limited sensitivity at very high speeds. The OCT system exhibits deep penetration into the choroid even for moderate applied laser power of around 1.5mW. The presented results suggest that currently FDML lasers may offer better speed performance in the 1050nm wavelength range than line scan cameras or short cavity swept lasers, which are currently restricted to around 100kHz and 200kHz single spot axial scan rates, respectively.

In conclusion, the ultra-rapid acquisition of ultrawide-field OCT data enabled by FDML based ultrahigh speed SS-OCT enables a series of new data analysis protocols which may impact clinical diagnosis in the future. The flexibility with respect to the extracted image orientation may suggest that a high imaging speed with slightly reduced sensitivity and subsequent averaging is preferred to slower imaging. The ultrahigh imaging speed may provide the ability to simplify clinical ophthalmic imaging. In some cases, the need for separate acquisition of images with fundus cameras or/and laser scanning ophthalmoscopes and an additional OCT scan might be replaced by a single ultrawide-field OCT scan such as presented here.

Acknowledgments

The authors would like to thank Dr. Aljoscha Neubauer, Profs. Rainer Leitgeb, Christoph Hitzenberger, Maciej Szkulmowski and Maciej Wojtkowski for helpful discussions, and acknowledge support from Prof. W. Zinth at the Ludwig-Maximilians-University Munich. We also thank the undergraduate student Rainer Szalata, for developing and building numerous tools and modules used for and in the experiments. This research was sponsored by the Emmy Noether program of the German Research Foundation (DFG - HU 1006/2-1) and the European Union project FUN OCT (FP7 HEALTH, contract no. 201880).

#139343 - $15.00 USD Received 7 Dec 2010; revised 17 Jan 2011; accepted 21 Jan 2011; published 2 Feb 2011
(C) 2011 OSA